The International Journal of Advanced Manufacturing Technology (2019) 103:3265–3278
https://doi.org/10.1007/s00170-019-03588-3

ORIGINAL ARTICLE

A mathematical model of laser cladding repair

Shichao Zhu[1] · Wenliang Chen[1] · Liping Ding[1] · Xiaohong Zhan[2] · Qi Chen[3]

Received: 20 August 2018 / Accepted: 12 March 2019 / Published online: 2 May 2019

Abstract

To obtain more accurate geometric features of laser cladding layer repair for Invar alloy, an integrated model of the laser cladding repair process is formulated and evaluated. The model evaluates geometric features, namely, the width, contact angle or height of cladding layer, and dilution rate for a given laser power, scanning speed, powder feed rate, and height of the cladding layer or contact angle. First, a model is presented that can ensure the powder from the nozzles melts completely before it hits the base material. Second, a model of the geometric characteristics of cladding layer is developed to determine how the scanning speed and powder feed rate affect the contact angle. Third, a model of the dilution rate is provided to account for the energy absorbed by the base material. The laser power which filters through the powder is absorbed by the base material. Then, the laser power is reflected by the base material, attenuated by the powder, and partly deflected back to the base material. In addition, the powder absorbs part of the attenuated power and surrenders it to the base material. Incidentally, the microstructure of the cladding layer responds to the super-cooling degree of the liquid-solid interface. The results show that the mathematical model is well supported by the experimental results.

Keywords Laser cladding repair · Invar alloy · Mathematical model

Nomenclature

r_p	Radius of powder particles (mm)
v_p	Powder particles velocity (mm/s)
ρ	Density of Invar alloy (g/mm^3)
a_w	Curve coefficient of cladding layer
C_p	Specific heat of Invar alloy (J/kg°C)
S_1	Cross-sectional area of cladding layer (mm^2)
T_0	Ambient temperature (°C)
w	Width of cladding layer (mm)
T_m	Melting temperature of Invar alloy (°C)
t	Time t that a powder particle is ejected from the nozzle to the base material (s)
l_p	Latent heat of melting (powder and base material material) (J/g)
h, h_s	Height of cladding layer; melting depth of base material (mm)
η_p	Utilization of powder particles
H	Distance between nozzle and base material (mm)
a_p	Absorptivity of powder particles
r_l	Laser beam diameter (mm)
P_l	Laser power (W)
r_{jet}	Radius of powder particles flow (mm)
P_{at}	Attenuation power (W)
n	Number of particles involved in shading
S_p	Projection of intersection surface between powder particles and beam on base material (mm^2)
θ_{jet}	Inclusion angle between powder particle flow and horizontal plane (°)
ε	Emissivity
V_{pfr}	Powder feeding rate (g/min)
σ	Stefan-Boltzman constant (W/ m^2·K^4)
S_l	Area of laser spot (mm^2)
h_c	Heat convection coefficient W/(m^2·°C)
V	Volume of powder particles injected from the nozzles before reaching the base material (mm^3)
θ	Contact angle of cladding layer (°)
a_s	Absorptivity of base material

✉ Liping Ding
lpding@nuaa.edu.cn

[1] College of Mechanical and Electrical Engineering, Nanjing University of Aeronautics and Astronautics, Nanjing 210016, People's Republic of China

[2] College of Material Science and Technology, Nanjing University of Aeronautics and Astronautics, Nanjing 211106, People's Republic of China

[3] China Academy of Engineering Physics, Mianyang 621054, People's Republic of China

k	Thermal diffusivity [W/(m·K)]
q	Heat flux density [J/(m^2·s)]
v	Laser scanning speed (m/min)
m_c	Mass of cladding layer on the base material (g)
a_h, b_h	Front length, rear length and half width of heat source model
c_h	
S_2	Cross-sectional area of molten pool of the base material (mm^2)
a_s	Curve coefficient of base material
D	Dilution rate
a	Distance between cladding layer and left side of base material (mm)
b	Distance between cladding layer and right side of base material (mm)
c, d	Width and height of base material (mm)
m_t	Mass of powder particles ejected from nozzles (g)

1 Introduction

The laser cladding repair (LCR) is a promising additive manufacturing technology. The laser beam passes through the powders injected from coaxial nozzles and then irradiates the base material, which leads to the melting and solidification of powder and base material surface [1, 2]. In the LCR, a laser beam is performed as a heating to scan the surface of the base material: a molten pool is created over an existing base material and the molten pool is filled with the cladding material simultaneously (i.e., in the process of single-pass cladding). Cladding layers result, with metallurgy integrated to the base material thanks to fusion and diffusion. The LCR can be laid, and the manufacture of a three-dimensional part is possible by the aid of consecutive pass-by-pass and layer-by-layer cladding. In comparison with subtractive technologies, waste is reduced. The LCR has a good many advantages: low heat input, limited heat effects on base material metal (HAZ), minimum thermal deformation, fast cooling rate, lower dilution rate, perfect metallurgical bonding between the base material and cladding layer, reduced cracking susceptibility, excellent mechanical properties, high accuracy of the geometric characteristics of the cladding layer, and suitability for full automation in contrast to the conventional welding processes [3, 4]. Therefore, the wonderful idea is to provide added cladding material over worn and damaged surfaces to return to required dimensions or shape, avoiding part abandonment. So, a number of parts with serious worn or damaged have been repaired by using the method of the LCR such as aerospace, automobile, defense, mold, petrochemical, and nuclear industries [5–7].

The various application of Invar alloy mold can bring many problems. In the process of welding assembly, problems like increases in porosity, crack formation, shrinking, and undercutting may arise [8]. During its machining of the process, it is hard to avoid exceeding dimension tolerance and producing overcut phenomenon. While using and transporting, the damages done to the mold like abrasion, material fatigue, cracking, and scratch may also appear. Therefore, a suitable remanufacturing technique that can repair the damaged and defective Invar alloy mold would be conducive to the recycling of the mold material, so then lowering the production costs, conserving resources, and protecting environment. Previously, a worn or damaged mold is generally repaired by the laser welding. Nevertheless, its welding layers embrace more defects and possess the inferior quality. A great many advantages have been recommended in the LCR comparing with conventional welding for repairing. As the laser energy is highly concentrated, the repaired parts can be implemented fast heating and rapid cooling and produce smaller thermal deformation, narrower heat affected zone, and lower residual stress [9–11]. However, holes, larger deformations, and other defects may occur in the cladding layer if the parameters are not appropriate [12–16]. Invar alloy contains a high amount of Ni element; the fluidity of molten pool of the liquid metals is insufficient, which can result in higher residual stress and lower strength between the cladding layer and base material. So, specific processing parameters are needed to achieve the desired quality and characteristics of the cladding layer.

In order to establish a model of the processing parameters of the LCR and to regulate the geometric features of the cladding layer, the LCR process, and outcome, a great deal of research on analytical and numerical models has been explored for calculation and simulation of the process. Cheikh et al. investigated that the geometric characteristics and dilution rate of the cladding layers have a weighty influence on the quality and performance of repair. In order to fully comprehend the nature of the process, control the geometric characteristics of the cladding layers, and perfect metallurgical bonding between the base material and cladding layer, numerous analyses and models of laser cladding have been performed to simulate the LCR [17]. Picasso et al. presented a foundational model to predict the laser scanning speed and powder feeding rate (injected from the nozzle) for a given height of cladding layer, laser radius, and laser power. Their research discussed the multi-track laser cladding and melt-pool shape and used three-dimensional modeling with the assumption that the particles had been pre-placed on the base material [18]. Ni et al. proposed a combination of the particle swarm optimization algorithms and back-propagation neural network to optimize the process parameters during the LCR. A desired neural network model that described the relationships between the height and width of the cladding layer and the technological parameters had been investigated. Therefore, a better relation between the technological parameters and the geometric features of the cladding layer was obtained [19]. Lalas et al. investigated a mathematical model of the geometry features of the cladding layer, which accounted for the calculation of the geometry characteristics of the cladding layer as the primary purpose for the surface tension between the cladding layer and

the base material [20]. Hussam et al. developed analytical relationships between the geometric features (area, width, height of cladding layer, and melting depth of the base material) and the process parameters (powder feeding rate injected from the nozzle, laser power, and laser scanning speed). Their work suggested that the analytical relations are implemented between the process parameters and the geometrical features and the shape of the cladding layer [21]. Hofman et al. dealt with a novel model to determine the dilution rate and geometrical characteristics of the cladding layer in the laser cladding. This model deals with the balance equations with regard to the mathematical transformation, which describes the physical effects and the correlativity between the dilution rate and the melt pool characteristics of cladding layer [22]. Caiazzo et al. arranged a full-factorial experimental plan and investigated geometry characteristics, microhardness, and heat-affected zone of cladding layer as functions of the significant governing process parameters, laser power, scanning speed, and particle velocity. In addition, the dilution rate and catching efficiency of powder particles by the molten pool have been assessed [23]. Zeng et al. established a thermal damage model as a function of material discontinuity, residual stress, microhardness to provide scientific quantitative analysis, and appraisal and investigated the mechanical behavior of the repaired specimens by using the technology of laser cladding to repair a V-groove [24].

It is worth taking any emerging technology seriously in the industry; a flexible mathematical model would be preferable to save some trial-and-error. Actually, a massive endeavor has been made to model the process of the LCR. Although the previous references show that there are a larger number of models, whose researches are limited to a certain process of laser cladding. In this paper, mathematical models have been proposed that consider the melting of particles, shading rate, geometric features, and dilution rate as a whole to develop an integrated model.

In this paper, an alternative mathematical analysis model is established to estimate the geometric characteristics of cladding layer (height h, width w, curve equation $f(x)$ dilution rate D in Fig. 1), which considers the laser-powder, laser-base material, and powder-base material interactions. Therefore, the energy absorbed by the base material is accounted for. Given the initial conditions and boundary conditions, the dilution rate of base material can be derived from the equation of heat conduction of the base material. The mathematical analysis models may be applicable to control and monitor the LCR process.

2 Mathematical model of the LCR

The model is established in following steps in order to estimate the geometric features of cladding layer:

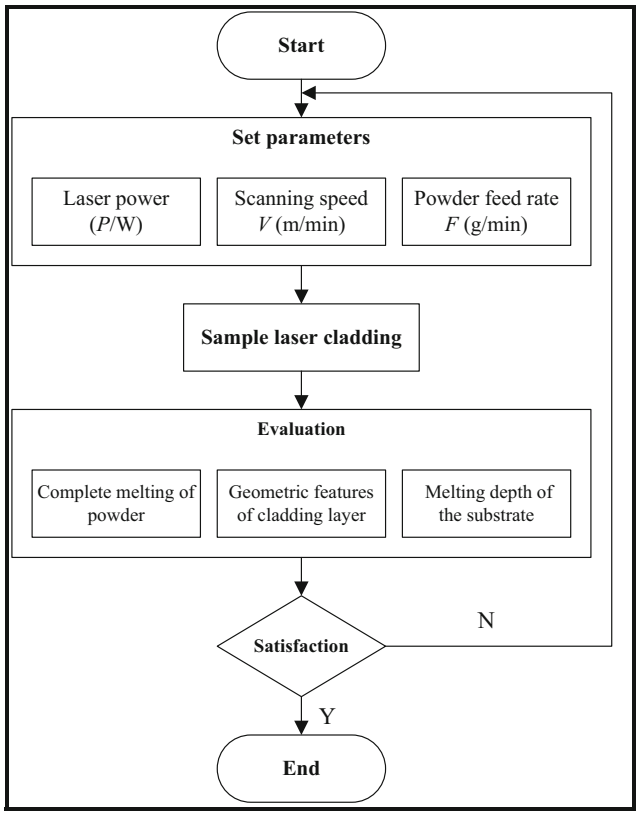

Fig. 1 Flow chart of the LCR

Step 1: How much energy can ensure the powder from the nozzles melts completely before it hits the base material.
Step 2: The equations of the profile curve, height, and width of cladding layers (Fig. 1) are determined.
Step 3: The dilution rate is calculated.

Figure 1 illustrates the flow chart of the LCR.

2.1 Energy required for melting particles

Whether the powder particles are melted completely plays vital roles on the performance and quality of cladding layer. Non-molten and limited molten powder particles do not affect the surface roughness of cladding layer, but also may generate pores that lead to the collapse of the cladding layer.

The model includes the following assumptions:

a. The size distribution of powder particles is uniform and their shape is all spherical with a radius of r_p.
b. Reflection, diffraction, as well as scattering of powder particles are neglected.

Ensure that the powder particle injected from the nozzle completely melted before it reaches the base material in the process of laser cladding. The energy E_p is as follows:

$$E_p = \frac{4}{3}\pi r_p^3 \rho\left[C_p(T_m - T_0) + l_p\right] \tag{1}$$

When the powder particles pass through the laser beam, the energy E_{ab} absorbed by the powder particle is as follows:

$$E_{ab} = 2\pi r_p^2 a_p \frac{P_l}{\pi r_l^2} t \tag{2}$$

As the laser beam passes through powder particles injected from a coaxial nozzle and then irradiates the base material, one part of laser beam is reflected by the base material and again is absorbed by the powder. Therefore, the energy E_r is as follows:

$$E_r = 2\pi r_p^2 \eta_p a_p (1 - a_s) P_l \left(1 - \frac{P_{at}}{P_l}\right)\frac{P_{at}}{P_l} t \tag{3}$$

The energy Q_r that a particle radiates can be presented:

$$Q_r = S_p \varepsilon \sigma \left(T_m^4 - T_0^4\right)\Delta t = 4\pi r_p^2 \varepsilon \sigma \left(T_m^4 - T_0^4\right)\Delta t \tag{4}$$

The energy Q_c in which a particle converts the heat to air can be presented:

$$Q_c = S_p h_c (T_m - T_0)\Delta t = 4\pi r_p^2 h_c (T_m - T_0)\Delta t \tag{5}$$

As a result, the heat balance equation of particles is as follows:

$$E_{ab} + E_r - Q_r - Q_c = E_p \tag{6}$$

The energy that can ensure the powder from the nozzles melts completely before it hits the base material is calculated by solving Eqs. (1)–(6).

2.2 Geometrical features of cladding layer

Under certain conditions, θ is assumed to be related to the nature of the material. So, the Fig. 2 shows the geometrical characteristics of the cladding layer.

The cross-sectional curve of cladding layer is given as

$$f(x) = a_w x^2 + b \tag{7}$$

The coordinates of x_0 and y_0 are $\left(-\frac{w}{2}, 0\right)$, $(0, h)$, respectively; therefore, the width of cladding layer is

$$w = 2\sqrt{\frac{h}{|a_w|}} \tag{8}$$

The contact angle is given as

$$\left.\frac{dy}{dx}\right|_{y=h} = tan\theta \tag{9}$$

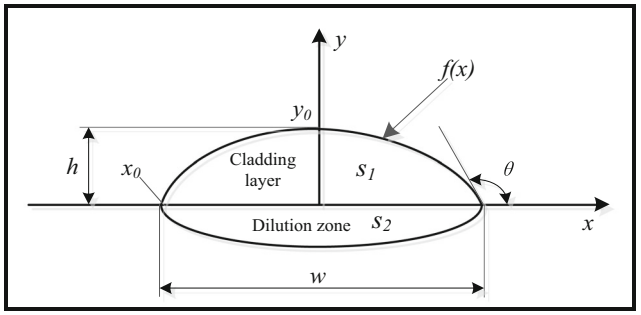

Fig. 2 Diagrammatic sketch of the geometrical features of cladding layer

$$\left.\frac{dy}{dx}\right|_{y=h} = \left.2a_w x\right|_{x=\sqrt{\frac{h}{|a_w|}}} = 2a_w\sqrt{\frac{h}{|a_w|}} = tan\theta \tag{10}$$

The height of cladding layer is as follows:

$$h = \frac{tan^2\theta}{4|a_w|} \tag{11}$$

The area of cladding layer is expressed as

$$S_1 = 2h\sqrt{\frac{h}{|a_w|}} - 2\int_0^{\sqrt{\frac{h}{|a_w|}}} a_w x^2 dx = \frac{4h}{3}\sqrt{\frac{h}{|a_w|}} = \left|\frac{tan^3\theta}{6a_w^2}\right| \tag{12}$$

Within time t, the mass of powder particles ejected from nozzles is certain:

$$m_t = V_{pfr}\,\mathrm{t} \tag{13}$$

Within time t, the mass of cladding layer on the base material is certain:

$$m_c = \rho\, V_p \tag{14}$$

The mass of powder utilization ratio is equal to the mass of cladding layer.

$$V_{pfrt}\eta = \rho\, V_p \tag{15}$$

The volume of cladding layer is equal to the product of its length and cross section area.

$$V_p = S_1\, h_p \tag{16}$$

The length of cladding layer is equal to the product of scanning speed and scanning time.

$$h_p = v\, t \tag{17}$$

Therefore, the cross-sectional area of cladding layer can also be expressed as

$$S_1 = \frac{V_{pfr}\frac{1}{v}\eta}{\rho} = \frac{V_{pfr}\,\eta}{\rho\, v} \tag{18}$$

The contact angle and width of cladding layer can be calculated by solving the Eqs. (7)–(18).

The cross-sectional area of cladding layer is measured: the data of surface profile of cladding layer are acquired by a non-contact measurement device. According to these points, the curve is determined.

2.3 Dilution rate

2.3.1 Attenuation model

Before the laser beam reaches the base material, the powder cloud shades a part of the laser beam and also attenuates part of the laser power. So, by calculating the shading rate, the laser power that passes through the powder cloud is absorbed by the base material that can be obtained.

The shading rate model includes the following assumptions:

a. The size distribution of powder particles is uniform and their shape is all spherical with a radius of r_p.
b. The particles do not overlap each other in the laser beam.
c. Reflection, diffraction, as well as scattering of powder particles are neglected.
d. The laser energy presents a uniformity of intensity distribution.

The diagram of the shading rate is presented in Fig. 3a, and the diagrammatic sketch of the interaction relations between powder particles and laser power is presented in Fig. 3b.

The time t that a powder particle is ejected from the nozzle to the base material (E_1E_2) is as follows:

$$t = \frac{H}{v_p sin\theta_{jet}} \tag{19}$$

The mass of powder particles injected from the nozzle in a time t is

$$m_t = V_{pfr} t = V_{pfr} \frac{H}{v_p sin\theta_{jet}} \tag{20}$$

The volume of the cylinder formed by the powder particles from the nozzle is

$$V_C = \pi r_{jet}^2 E_1E_2 = \pi r_{jet}^2 \frac{H}{sin\theta_{jet}} \tag{21}$$

The volume of *BGMF* held by the powder particles is as follows:

$$V_p = \pi r_l^2 E_2\mathrm{C} = \pi r_l^2 \frac{E_2\mathrm{D}}{\cos\theta_{jet}} = \pi r_l^2 \frac{r_{jet}}{\cos\theta_{jet}} \tag{22}$$

The powder particles are assumed that they are evenly distributed in the space, so the mass of powder per unit volume is

$$m_o = \frac{m_t}{V_C} = V_{pfr} \frac{H}{v_p sin\theta_{jet}} \quad \frac{sin\theta_{jet}}{\pi r_{jet}^2 H} = \frac{V_{pfr}}{v_p \pi r_{jet}^2} \tag{23}$$

The mass of the powders involved in the shading rate is as follows:

$$n \frac{4\pi r_p^3 \rho_p}{3} = m_o V_p \tag{24}$$

The total areas of all the particles in the laser beam and the area of the laser spot are as follows, respectively.

$$S_p = n\pi r_p^2 = \frac{3 v_{pfr} r_l^2}{4 v_p r_p r_{jet} \rho cos\theta_{jet}}; \quad S_l = \pi r_l^2 \tag{25}$$

Therefore, the rate of shading is as follows:

$$\frac{P_{at}}{P_l} = \frac{S_p}{S_l} = \frac{3 V_{pfr}}{4\pi r_p \rho v_p r_{jet} cos\theta_{jet}} \quad \left(r_{jet} \geq r_l\right) \tag{26}$$

In these experiments, the radius of powder particle r_p, the velocity of carrier gas v_p, the inclusion angle between powder particle flow and horizontal plane θ_{jet}, and the radius formed on the base material by the powder particles r_{jet} are 120 μm, 600 mm/min, 55°, and 8 mm, respectively. The powder feeding rates F are 5 g/min, 7 g/min, and 9 g/min and the shading rates are 46.04%, 64.46%, and 82.88%, respectively.

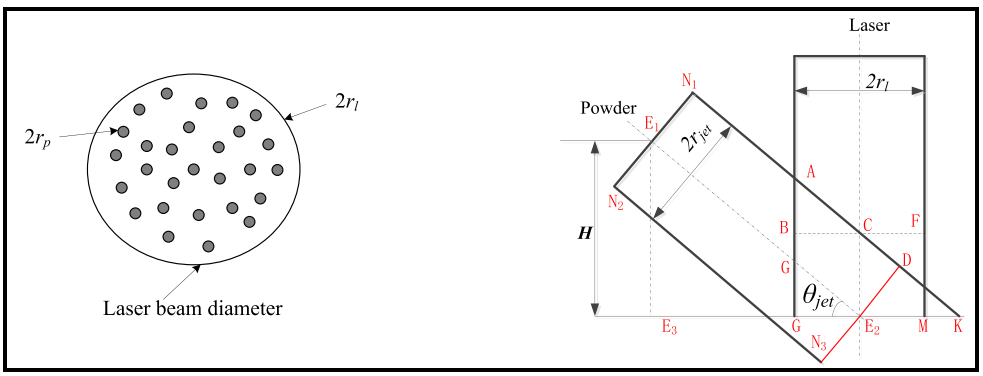

(a) Shading rate (b) Interaction between particles

Fig. 3 Diagrammatic sketch of the interaction between particles and laser. **a** Shading rate. **b** Interaction between particles

2.3.2 Energy obtained by base material

Before the powder is injected from the nozzles to the base material, it will attenuate part of the laser power. So, the laser power which is absorbed by base material is as follows:

$$E_s = a_s P_l \left(1 - \frac{P_{at}}{P_l}\right) \tag{27}$$

During the time that the powder passes through the laser beam, it will absorb part of laser power and surrender it to the base material. Then, the powder strikes and enters into a molten pool.

$$E_m = \eta_p a_p P_l \frac{P_{at}}{P_l} \tag{28}$$

The base material reflected part of laser beam and was again absorbed by the powder when the laser beam passed through the powder cloud and irradiated the base material. Therefore, the reflected power transferred back to the base material is as follows:

$$E_r = \eta_p a_p (1 - a_s) P_l \left(1 - \frac{P_{at}}{P_l}\right) \frac{P_{at}}{P_l} \tag{29}$$

2.3.3 Melting depth of base material

Figure 4 presents the heat conduction process of the laser cladding. The system of Eqs. (25)–(32) can be solved by the MATLAB.

The heat conduction equation is as follows:

$$k\left(\frac{\partial^2 T}{\partial x^2} + \frac{\partial^2 T}{\partial y^2} + \frac{\partial^2 T}{\partial z^2}\right) + q = \rho C_p \frac{\partial T}{\partial t} \tag{30}$$

The laser power distribution profile is as follows:

$$q(x,y,z) = \frac{6\sqrt{3}Q}{a_h b_h c_h \pi \sqrt{\pi}} \exp\left(-\frac{3(x-a)^2}{a_h^2} - \frac{3(y-vt)^2}{b_h^2} - \frac{3(z-d)^2}{c_h^2}\right) \tag{31}$$

$0 < x < a + b$, $0 < y < c$, $0 < z < d$, $0 < x < a + b$, $t > 0$.

B. C.

$$-\frac{\partial T}{\partial x} + H_{x1} T = 0, x = 0, t > 0 \tag{32}$$

$$\frac{\partial T}{\partial x} + H_{x2} T = 0, x = a + b, t > 0 \tag{33}$$

$$-\frac{\partial T}{\partial y} + H_{y1} T = 0, y = 0, t > 0 \tag{34}$$

$$\frac{\partial T}{\partial y} + H_{y2} T = 0, y = c, t > 0 \tag{35}$$

$$-\frac{\partial T}{\partial z} + H_{z1} T = 0, z = 0, t > 0 \tag{36}$$

$$\frac{\partial T}{\partial z} + H_{z2} T = 0, z = d, t > 0 \tag{37}$$

$$T(x,y,z) \geq 1450^{\circ}\mathrm{C} \tag{38}$$

I. C.

$$T_{amb} = 20^{\circ}\mathrm{C}, t = 0, 0 < x \leq a + b, 0 \leq y \leq c, 0 \leq z \leq d \tag{39}$$

2.3.4 Calculation of dilution rate

The curve coefficient of the base material-melting region is as follows:

$$a_s = \frac{|4h_s|}{w^2} \tag{40}$$

The area of the base material-melting region is as follows:

$$S_2 = 2|h_s|\sqrt{-\frac{h_s}{a_s}} - 2\int_0^{\sqrt{-\frac{h_s}{a_s}}} a_s x^2 dx = \frac{4|h_s|}{3}\sqrt{-\frac{h_s}{a_s}} = \frac{2w|h_s|}{3} \tag{41}$$

The melting width and penetration depth of the base material deduced from the metallographic microscope measurements are employed for determining the melting area of the base material, as shown in Eqs. (30)–(41).

The dilution rate (Fig. 2) is as follows:

$$D(\%) = \frac{S_2}{S_1 + S_2} \tag{42}$$

3 Experiment

3.1 Experimental material

The raw material was produced by the French Pulang Alloy Co., Ltd. (Paris, France) and was offered by Commercial Aircraft Corporation of China Ltd. (Shanghai, China). Then, the material was processed for the LCR experiments. According to the experimental requirements, the base material was manufactured: the length ×width width ×height sizes of the base material were 100 mm ×50 mm ×20 mm, respectively. In addition, the Invar alloy powder was prepared by the method of plasma rotating electrode. The chemical compositions of the base material and powder particles are presented in Table 1. The Table 2 particularizes the natures of the Invar alloy applied in the LCR. The Fig. 5a well provides information on chemical composition of the base material and powder particles by use of X-ray spectrometer attachments. The morphological evaluation (detection of size and shape) of the

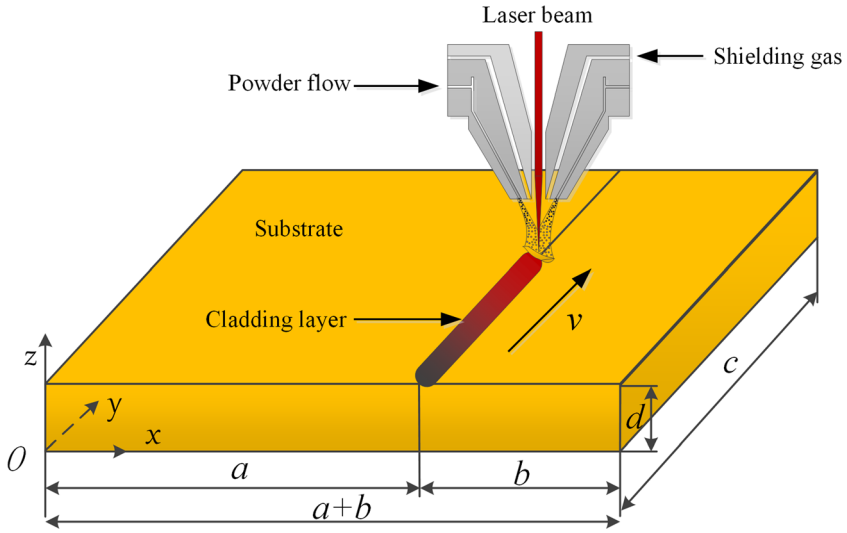

Fig. 4 Calculation of heat conduction in the LCR process

powder particles were conducted employing a scanning electron microscope, namely SEM (BRUKER, Germany), and the radii of the powder particles were performed to be in the range of 50–150 μm, as presented in Fig. 5b.

3.2 Experimental equipment and methods

The LCR equipment comprises a LCR system with a 6 kW continuous Nd:YAG laser (TRUMPF, Germany), a coaxial powder feeding system, a CNC system, and a gas protection system, as presented in Fig. 6a.

After the LCR experiments, each cross-sections of the cladding layer was cut by wire electric discharge machining (EDM) and was then ground, polished by the carborundum papers of different particle sizes and polishing machine, respectively. Next, the information on the microstructure of the each cladding layers was provided by use of the Leica metallographic microscope, as shown in Fig. 6b. The available measuring and testing of the non-contact optical profiler (Sensofar, Spain) extract the geometrical characteristics with regard to the width, height, and cross-section profile of the cladding layers by use of the white light interferometry as reliable data for theoretical analyses.

The temperature and humidity have great influence on the Invar alloy, so the Invar alloy is inclined to rust. First, the surface of the base material was processed by use of the milling machine, and subsequently, cleaning as well as drying was performed. Then, during the LCR, the powder particles and base material were put in sealed cabin by use of the argon as a shielding gas to prevent their oxidation. Prior to the LCR, to exhaust the air thoroughly, the shielding gas flow rate was 15 L/min and was vented for approximately 25–30 min in the sealed cabin. Besides, a 5-diameter laser beam spot was formed on the base material by adjusting the defocusing amount. The experimental process parameters and results of the LCR are performed in Table 3.

Table 1 Chemical composition of the Invar alloy

Ni	Cr	Fe	Co	Mn	Si	C	P	S
35.92	0.20	63.0	0.47	0.27	0.07	0.025	0.0087	0.001

4 Results and discussion

4.1 Geometrical features analysis of cladding layer

For testing and verifying the experimental results of geometrical features of cladding layer and considering the effect of various process parameters, a series of experiments were performed. Figure 7 shows the experimental measurements of the ultrasound detecting results of the fourth group of cladding layer. The ultrasonic testing results of the seventh cladding layer can be noted, including X scan, C scan, and B scan. First, the cladding layer with height of 10 mm is scanned with X scan, which is sliced into 10 layers ($x_1, x_2 \ldots x_{10}$) and each layer is 0.12 mm. Then, the results of 10-layer X scan are projected to the ground surface to form C scan. The cladding layer is scanned with B scan along the longitudinal direction from the top of cladding layer. The results show that the cladding layer is black except the edge, which is white: in other words, no cracks or pores were detected in the random cross-sections of samples. Therefore, the quality of the cladding layer can satisfy the requirements.

Figures 8, 9, and 10 show the experimental measurements of the ultrasound detecting results, fitted curves, height, and width of the first group and dilution ratio of cladding layer.

Figure 11 compares the experimental with theoretical results, which are both in good agreement with each other even though there are some discrepancies between them. Known from the Figs. 8 and 11a, the value of a ($f(x) = ax^2$, quadratic

Table 2 Properties of the Invar alloy

Density g cm^{-3}	Thermal conductivity W · (m K)$^{-1}$	Modulus of elasticity MPa	Hardness HV	Tensile strength σ_b/MPa	Elongation δ/%
8.12	0.109~0.134	134,000	140	500	30

curve coefficient) deviation fluctuates between 0.8% for high power, lower powder feeding rates, and scanning speed, and 8.5% for lower power, higher powder feeding rates, and scanning speed. In summary, both experimental measurement results and theoretical calculation results reach a good agreement. Known from Eq. 1, the η (powder using efficiency) is attributed to the deviation. The radius of the powder that is formed on the base material is certain. The greater the width of the molten pool, the higher the utilization ratio of the powder. For a low scanning speed, lower powder feed rates and high power, the model calculates a slightly higher for the value of a, which was not matched with the experiments since the width of cladding layer was supported by the size and shape of the molten pool of the base material. As the scanning speed and lower powder feeding rate increase, the power decreases, leading to a smaller width of the cladding layer. Therefore, the restrictions of the size and shape of the molten pool of the base material influence the increased rate of the width of cladding layer. Furthermore, the point data collected from the cladding layer are measuring inaccuracies and approximately fitted by parabola, resulting in the deviation of the value of a.

Figure 9 illustrates the measurement of the height and width of cladding layer. This model estimates the height of cladding layer with a deviation varying between 0.8 and 9.3% in Fig. 11b. According to Eq. 1, the deviation was dominated by the value of a. Similarly, the deviation of the width was created by the deviation of height and parabola fitting, whose deviation varies between 0.9 and 8.6% in Fig. 11c.

The measuring results of the dilution rate are presented in Fig. 10. The seventh group with a value of 13.8% had the lowest dilution rate, as presented in Fig. 10g. The eighth group with a value of 72.2% had the highest dilution rate, as presented in Fig. 10h. Comprehensive consideration of the roughness, width, contact angle, height of cladding layer, as well as overlap ratio of the adjacent passes, the seventh group is the best. Figure 11d indicates that the theoretical results of the dilution rate are closely consistent with the experimental values. The model calculates the dilution rate with a deviation fluctuating between 5.4% for lower power, high powder feeding rates, and 15.7% for high power, low powder feeding rates when contrasted with the experimental data. These deviations are primary facts that the mathematical model evaluates the dilution rate, without entirely giving consideration to the effect of the convection and radiation on the base material and powder. As the laser power increases or the powder feed rates decrease, more energy is absorbed by the base material, resulting in the greater convection and radiation; hence, the dilution rate is underestimated and the deviation is significant. Subsequently, to a certain extent, the probable account for the discrepancy may be attributed to the alteration of the Invar alloy material properties (specific heat capacity, thermal conductivity, and so on) under different temperature conditions, which are all considered as constants in the calculation. What is more, the deviation may arise from the experimental error and measurement accuracy. Compared with the width and height of cladding layer, the melting depth of the base material

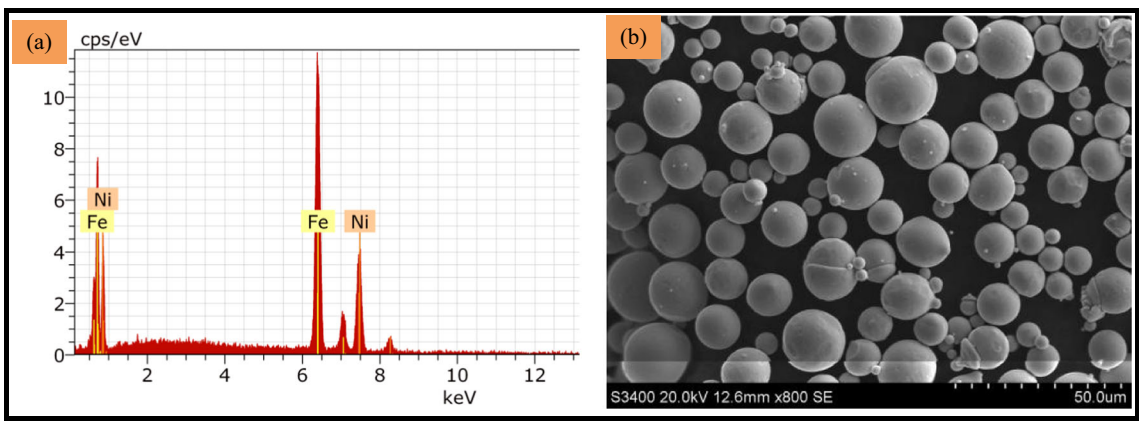

(a) Elemental composition measured via energy-dispersive X-ray spectroscopy (EDX)

(b) Morphology of the Invar alloy powder

Fig. 5 Elemental composition and Morphology of the Invar alloy powder. **a** Elemental composition measured via energy-dispersive X-ray spectroscopy (EDX). **b** Morphology of the Invar alloy powder

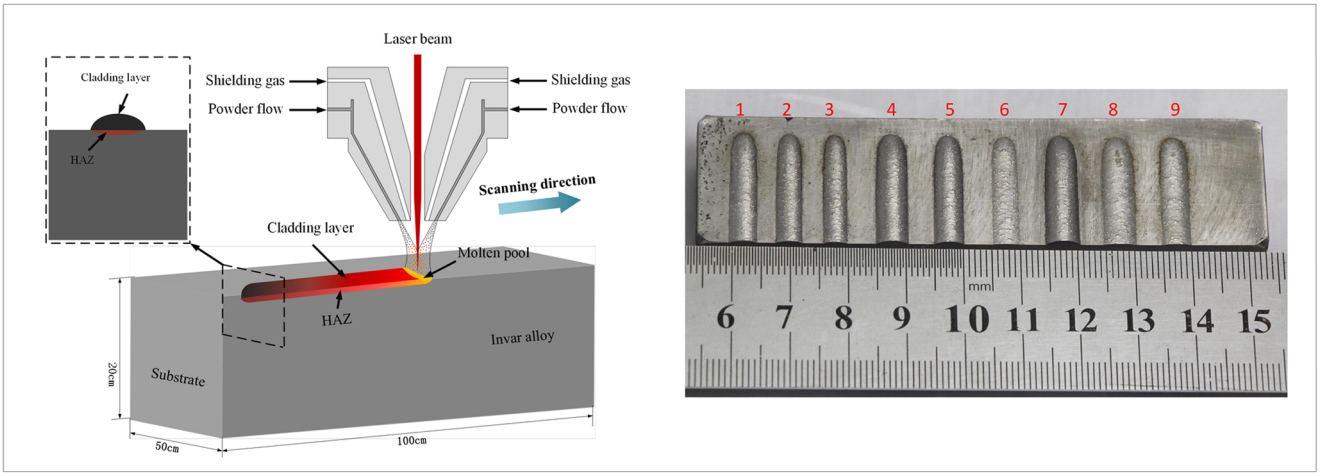

(a) Diagrammatic sketch of the LCR process (b) LCR specimens

Fig. 6 Single-pass and single-layer of the LCR. **a** Diagrammatic sketch of the LCR process. **b** LCR specimens

is harder to determine as a result of the unclear parting line between the molten pool and base material.

4.2 Microstructure analysis of cladding layer

Figure 12 presents the microstructure of cross-section of laser cladding layer of Invar alloy. Figure 12a presents the microstructures of different regions near the fusion line while Fig. 12b shows the cladding layer microstructure. As presented in Fig. 12a, the deposition layer primarily consisted of the cladding layer, heat-affected zone (HAZ), and base material. Due to the thermal cumulative effect, the grains in the unmelted regions near the fusion line swallowed each other, forming clear and coarse HAZ. The widening of HAZ was caused by the failure of timely dissipation of the heat absorbed by the cladding layer and base material owing to a large amount of instantaneous energy input and low thermal conductivity coefficient of the nickel-based alloy. Also, the microstructure near the fusion line, i.e., at the bottom region of the cladding layer, was dominated by the columnar crystals which grew inwards perpendicular to the fusion line, while the top of the cladding layer was dominated by the equiaxed crystals. Also, as shown in Fig. 12b, the columnar crystals and equiaxed crystals were composed of finer subgrains with the morphology of elongated cellular crystals and equiaxed cellular crystals. The refinement of the subgrains was due to rapid heating and cooling in the process of LCR.

The variation of subgrain morphology in different regions of cladding layer is mainly related to the compositional undercooling degree of the liquid phase. The compositional undercooling degree can be determined by the criterion equation of liquid composition stability:

$$\frac{G}{R} \geq \frac{-\mathrm{m}LC0(1-k)}{DLk}$$

The critical condition of the composition undercooling is given by

Table 3 Processing parameters and experimental results of the LCR of the Invar alloy

Track	Process parameters			Experimental results	
	Laser power P (W)	Scanning speed V (m/min)	Powder feeding rate F (g/min)	Height h (mm)	Width w (m)
1	1900	3	5	0.77	5.01
2	1900	5	7	0.81	4.59
3	1900	7	9	0.63	4.22
4	2100	3	7	1.21	5.70
5	2100	5	9	1.09	5.23
6	2100	7	5	0.29	4.75
7	2300	3	9	1.68	5.95
8	2300	5	5	0.47	5.68
9	2300	7	7	0.45	4.98

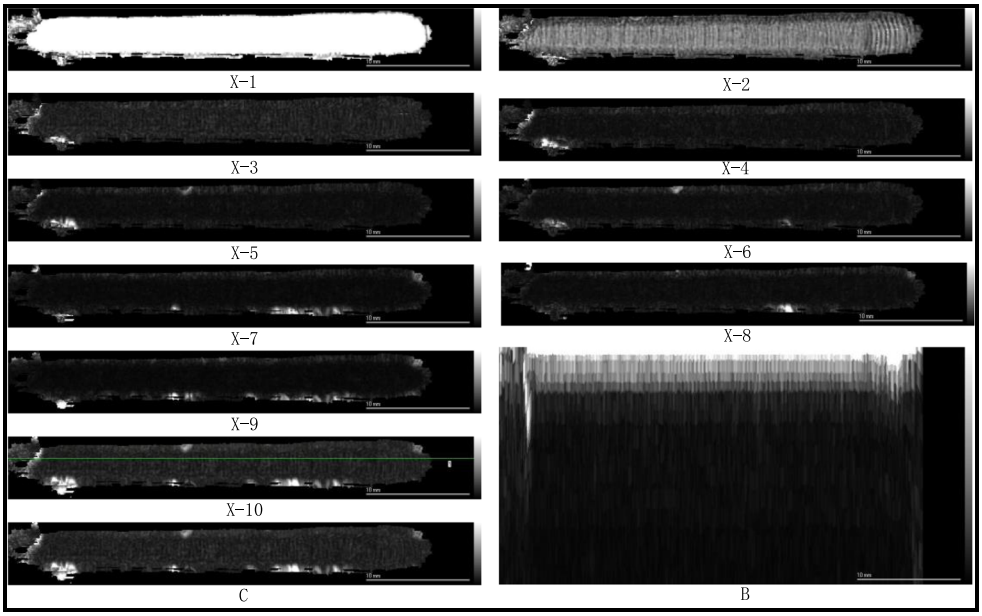

Fig. 7 Ultrasound detecting results of cladding layer

$$GC = \frac{\mathrm{m}LC0(1-k)}{DLk}R$$

If G is the actual liquidus temperature gradient, the composition undercooling occurs under the conditions of $G \leqq G_C$ and disappears when $G \geqq G_C$.

At the initial stage of the solidification of the molten pool, existing adjacent to the fusion line, the solidification rate of the melt at the solid/liquid interface was almost zero because the liquid metal remained in contact with base material. The value of G_C was extremely small and much lower than the liquidus temperature gradient. Therefore, no composition undercooling occurred, and hence, the grains grew in the form

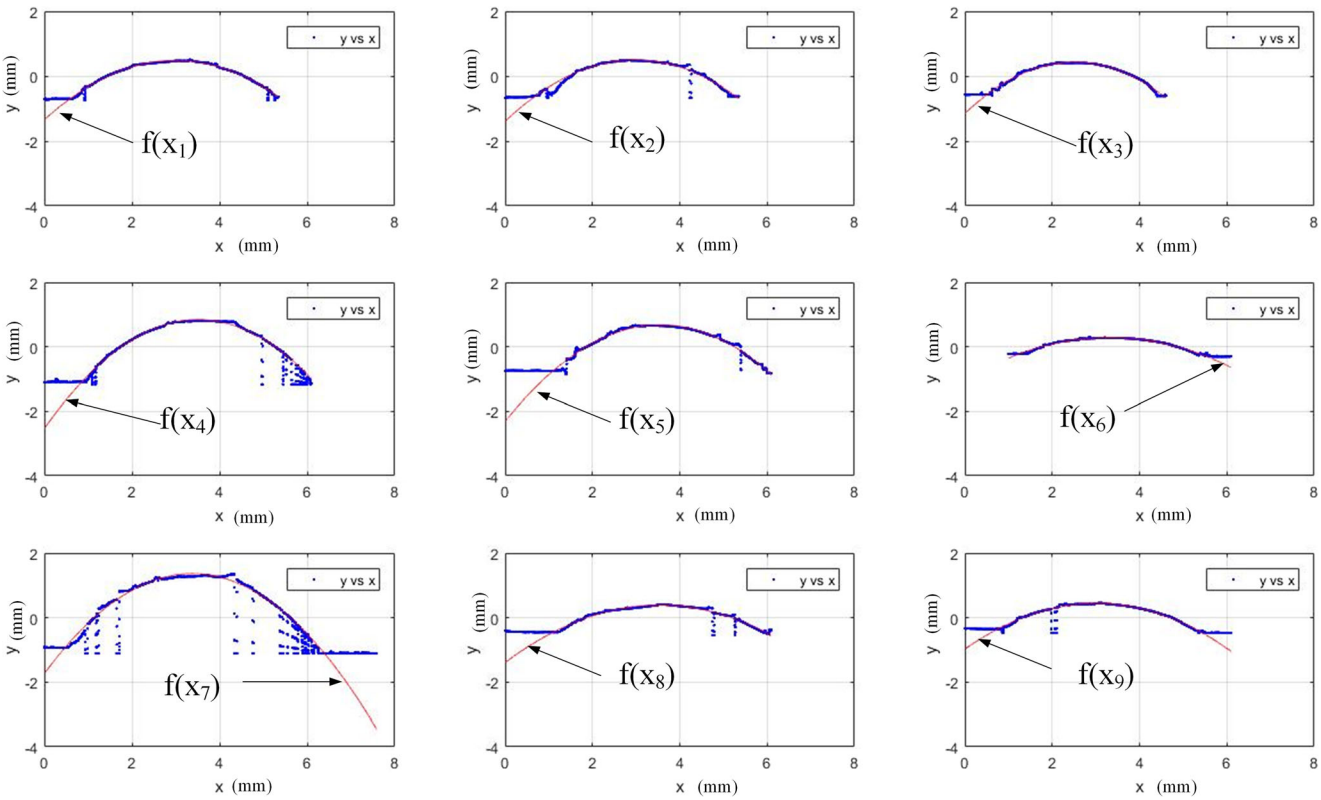

Fig. 8 Fitted curves of cladding layer

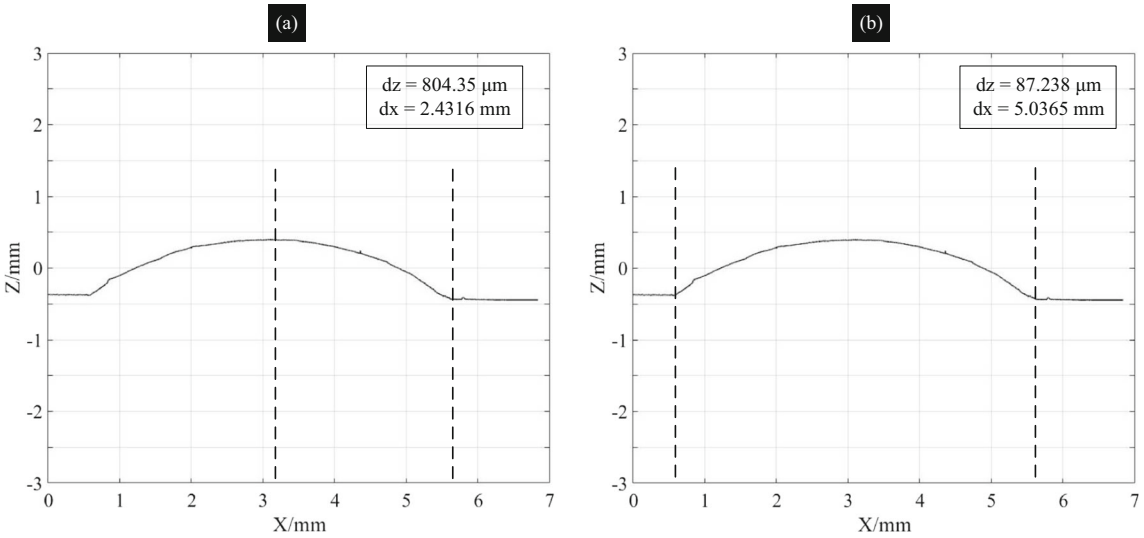

Fig. 9 Height and width measurements of the first cladding layer

of plane crystals. However, the duration of this morphology was little and almost invisible. With the solidification process, heat accumulated at the front end of the solid/liquid interface. The temperature gradient, G, at the front end of solid/liquid interface decreased, while the solidification rate of the liquid metal increased rapidly, resulting in an increase in $G_{C.}$ When G_C exceeded the temperature gradient G, the composition undercooling occurred leading to the formation of elongated cellular crystals. As the undercooling degree further increased, the cellular crystals near the top of the cladding layer were transformed into the equiaxed cellular crystals (see Fig. 12b). The growth direction of the elongated cellular crystals near the fusion line was perpendicular to the solid/liquid interface and consistent with the growth direction of the large columnar grains. This is because at the initial stage of solidification, the direction of the maximum temperature gradient in the

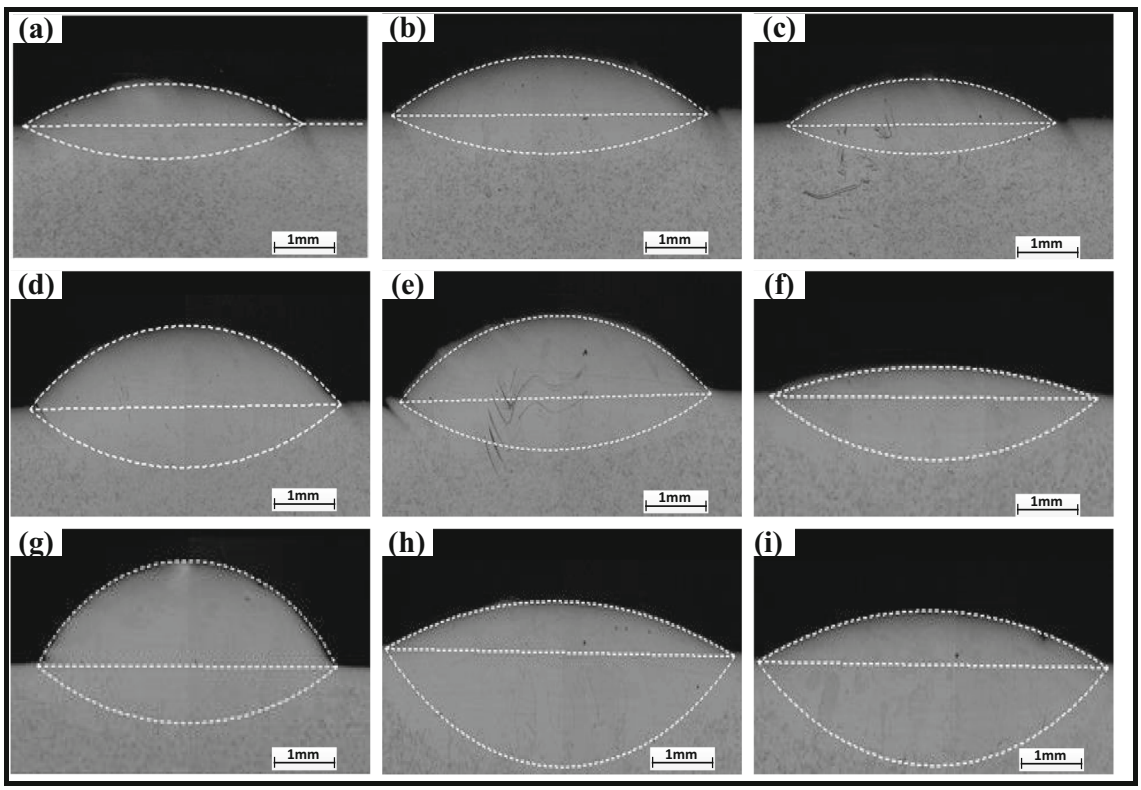

Fig. 10 Dilution ratio

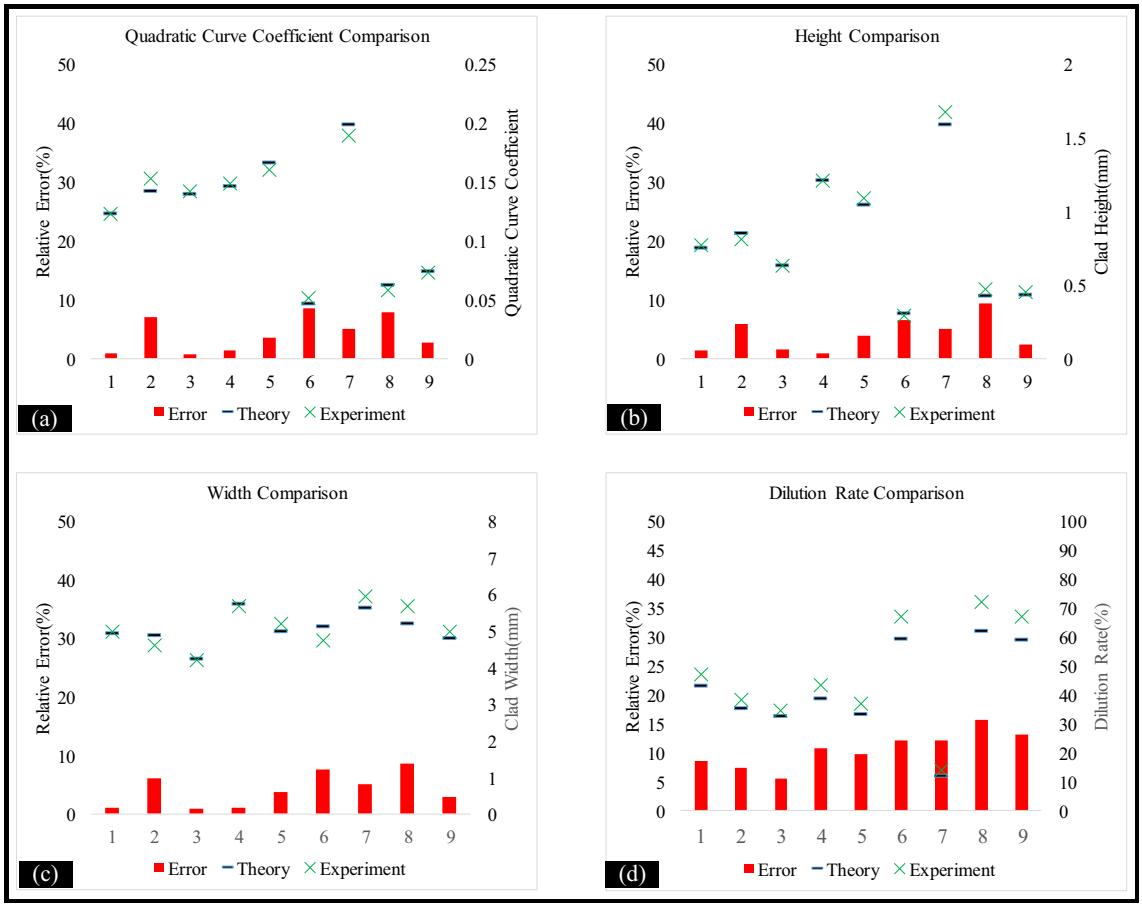

Fig. 11 Comparison of experimental value and theoretical value

molten pool, i.e., the fastest solidification direction, was normal to the fusion line, along which direction the grain growth had advantages. The huge advantages of grain growth in this direction led to the full growth of subgrains in this direction, forming a thin and elongated morphology.

As shown in Fig. 12b, the cellular crystals at the top of the cladding layer were mainly equiaxed cellular crystals that were slightly thinner without a clear directionality. This is mainly because when the near surface liquid metal solidified, the direction of the temperature gradient was environment-dependent. A large temperature difference between the liquid metal and environment led to a high solidification rate of the near surface liquid metal, a relatively low G/R value, and further refinement of the microstructure, leading to fine subgrains. Owing to the external heat exchange, the direction of the maximum temperature gradient was not perpendicular

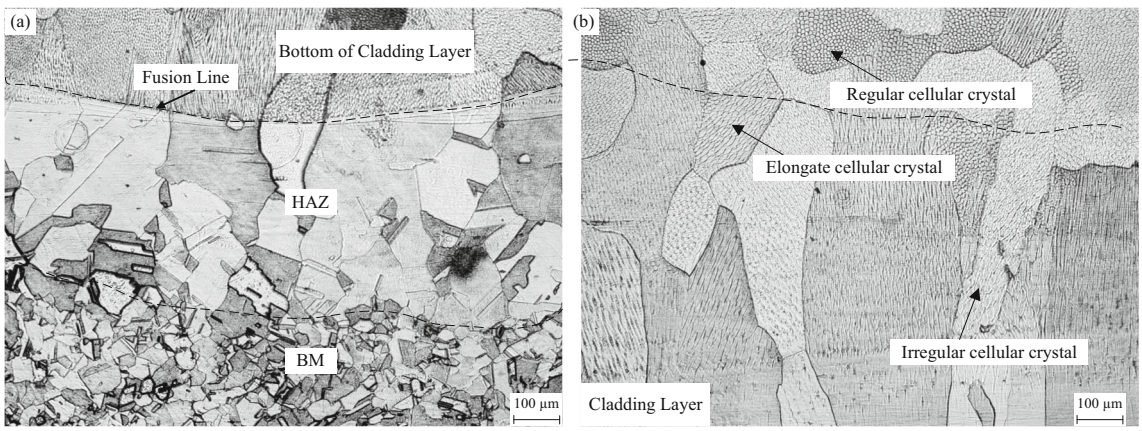

Fig. 12 Microstructure of cladding layer

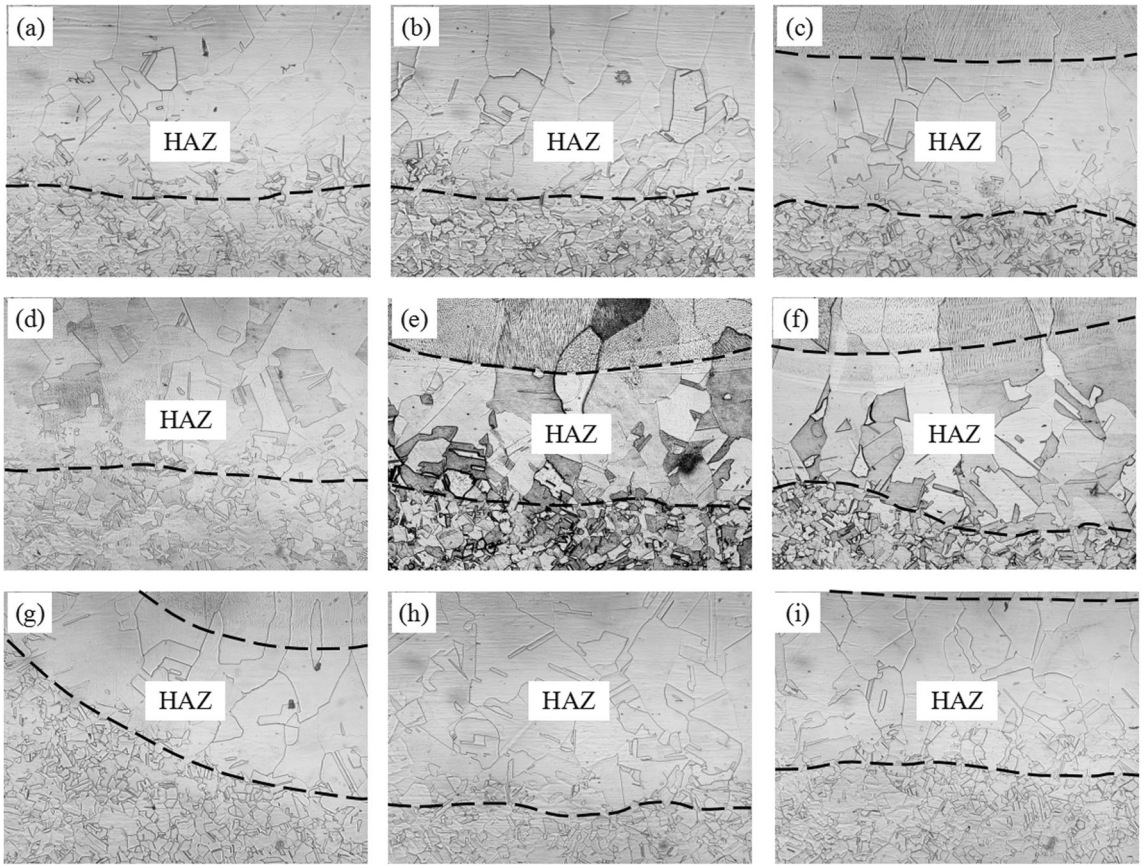

Fig. 13 HAZ of the cladding layer

to the solid/liquid interface, and hence, the directionality of subgrain growth was not clear.

Typical martensitic microstructures with a small amount of austenite and residual ferrite were found in the HAZ microstructure. Because of the high energy density, the temperature exceeded the austenitization temperature even in the unmelted regions of the molten pool edge. Owing to a sharp drop in temperature of HAZ caused by the rapid cooling of LCR, most of the austenites were directly transformed into martensites. However, in the areas far from the heat source, the microstructures did not change significantly and still composed of pearlite and ferrite.

As shown in Fig. 13, the narrowest HAZ of base material was achieved at the scanning speed of 3 m/min, powder feeding rate of 9 g/min, and laser power of 2300 W. We found that the width of HAZ depended upon the combined effect of the laser power, scanning speed, and powder feeding rate. In spite of heat input of laser cladding increasing with the increase of laser power, the decrease of scanning speed reduced the time of laser acting on the unit area, increasing the thermal accumulation. In addition, the increase in powder feeding rate resulted in more powders reacting with the laser, causing a greater reduction of laser power and hence, reducing laser on the matrix. Owing to the combined influence, the HAZ in Fig. 13g was relatively small.

5 Conclusion

An integrated mathematical model proposed in this paper may be used to determine the profile curves, height, width, dilution rate of cladding layer. The theoretical method indicates maximum deviation of 8.5% for the profile curves of cladding layer, 9.3% for the height, 8.6% for the width, 15.7% for the dilution rate for the LCR. Thus, the accuracy of the geometric characteristics of cladding layer and the melting depth of the base material are improved in the analytical model.

Certain processing parameters are more suited for liquid metal crystals and contribute to a more noticeable directionality in the microstructure in the cladding layer.

This integrated model gives us an insight into the whole process of the LCR. This theoretical method can be guidance for the process parameters that monitor and govern the LCR, particularly the geometric characteristics of cladding layer and the melting depth of the base material. Depending on the size of the defective Invar alloy mold for a special remanufacture, the process parameters can be adjusted accordingly to satisfy the needs of the LCR.

The microstructure near the fusion line at the bottom region of the cladding layer was dominated by the columnar crystals which grew inwards perpendicular to the fusion line, while the top of the deposition layer was dominated by the equiaxed

crystals. Moreover, the refinement of the subgrains was due to rapid heating and cooling in the process of the LCR.

Funding information Financial support of the project was received from the open fund of the State Key Laboratory of Additive Manufacturing, China academy of engineering physics (ZM17002) and the Key Laboratory of High and New Technology Project of Changzhou (CM20183004).

References

1. Gu DD, Meiners W, Wissenbach K, Poprawe R (2013) Laser additive manufacturing of metallic components: materials, processes and mechanisms. Int Mater Rev 57(3):133–164
2. Weng F, Chen C, Yu H (2014) Research status of laser cladding on titanium and its alloys: a review. Mater Des 58(6):412–425
3. Sexton L, Lavin S, Byrne G, Kennedy A (2002) Laser cladding of aerospace materials. J Mater Process Technol 122(1):63–68
4. Wang X, Sun W, Chen Y, Zhang J, Huang Y, Huang H (2018) Research on trajectory planning of complex curved surface parts by laser cladding remanufacturing. Int J Adv Manuf Technol 96(5–8):2397–2406
5. Shepeleva L, Medres B, Kaplan WD, Bamberger M, Weisheit A (2000) Laser cladding of turbine blades. Surf Coat Technol 125(1):45–48
6. Xu L, Cao H, Liu H, Zhang Y (2017) Study on laser cladding remanufacturing process with FeCrNiCu alloy powder for thin-wall impeller blade. Int J Adv Manuf Technol 90(5–8):1383–1392
7. Penaranda X, Moralejo S, Lamikiz A, Figueras J (2017) An adaptive laser cladding methodology for blade tip repair. Int J Adv Manuf Technol 92(3):1–7
8. Yu J, Kim D (2018) Effects of welding current and torch position parameters on minimizing the weld porosity of zinc-coated steel. Int J Adv Manuf Technol 95(1–4):551–567
9. Moralejo S, Penaranda X, Nieto S, Barrios A, Arrizubieta I, Tabernero I, Figueras J (2017) A feedforward controller for tuning laser cladding melt pool geometry in real time. Int J Adv Manuf Technol 89(1–4):1–11
10. Farshidianfar MH, Khajepour A, Gerlich A (2016) Real-time control of microstructure in laser additive manufacturing. Int J Adv Manuf Technol 82(5–8):1173–1186
11. Zheng H, Cong M, Dong H, Liu Y, Liu D (2017) CAD-based automatic path generation and optimization for laser cladding robot in additive manufacturing. Int J Adv Manuf Technol 92(9–12):1–10
12. Song L, Bagavath-Singh V, Dutta B, Mazumder J (2012) Control of melt pool temperature and deposition height during direct metal deposition process. Int J Adv Manuf Technol 58(1–4):247–256
13. Fathi A, Khajepour A, Toyserkani E, Durali M (2007) Clad height control in laser solid freeform fabrication using a feedforward PID controller. Int J Adv Manuf Technol 35(3–4):280–292
14. Alam MK, Urbanic RJ, Nazemi N, Edrisy A (2018) Predictive modeling and the effect of process parameters on the hardness and bead characteristics for laser-cladded stainless steel. Int J Adv Manuf Technol 94(1–4):397–413
15. Cheng YH, Cui R, Wang HZ, Han ZT (2017) Effect of processing parameters of laser on microstructure and properties of cladding 42CrMo steel. Int J Adv Manuf Technol 96(5–8):1–10
16. Verdi D, Múnez CJ, Garrido MA, Poza P (2017) Process parameter selection for Inconel 625-Cr3C2 laser cladded coatings. Int J Adv Manuf Technol 92(5–8):1–10
17. Cheikh HE, Courant B, Hascoët JY, Guillén R (2012) Prediction and analytical description of the single laser track geometry in direct laser fabrication from process parameters and energy balance reasoning. J Mater Process Technol 212(9):1832–1839
18. Picasso M, Marsden CF, Wagniere JD, Frenk A, Rappaz M (1994) A simple but realistic model for laser cladding. Metall Mater Trans B 25(2):281–291
19. Ni L, Liu J, Wu Y, Yan C (2011) Optimization of laser cladding process variables based on neural network and particle swarm optimization algorithms. Chin J Lasers 38(2):1–6
20. Lalas C, Tsirbas K, Salonitis K, Chryssolouris G (2007) An analytical model of the laser clad geometry. Int J Adv Manuf Technol 32:34–41
21. Cheikh HE, Courant B, Branchu S, Hascoët JY, Guillén R (2012) Analysis and prediction of single laser tracks geometrical characteristics in coaxial laser cladding process. Opt Lasers Eng 50:413–422
22. Hofman JT, Lange DF, Pathiraj B (2011) FEM modeling and experimental verification for dilution control in laser cladding. J Mater Process Technol 211:187–196
23. Caiazzo F, Alfieri V (2018) Laser-aided directed energy deposition of steel powder over flat surfaces and edges. Materials 11(3)
24. Zeng C, Tian W, Liao WH, Liang H (2013) Study of laser cladding thermal damage: a quantified microhardness method. Surf Coat Technol 236(24):309–314